

Thermally induced changes of structure in $\text{Ni}_{50}\text{Mn}_{25+x}\text{Ga}_{25-x}$ magnetic shape memory single crystals with very low twinning stress

L. Straka^{1,*}, J. Drahokoupil², O. Pacherová², K. Richterová², V. Kopecký²,
H. Hänninen¹, and O. Heczko²

November 7, 2014

¹ Aalto University School of Engineering, Laboratory of Engineering Materials, PO Box 14200, FIN-00076 Aalto, Finland

² Institute of Physics ASCR, Na Slovance 1999/2, 182 21 Prague, Czech Republic

Abstract

In search for the origins of the extraordinary low twinning stress of Ni-Mn-Ga magnetic shape memory alloys we studied the thermally induced changes of structure in $\text{Ni}_{50}\text{Mn}_{25+x}\text{Ga}_{25-x}$ ($x=2.7-3.9$) single crystal samples and compared them with twinning stress dependences. The alloys exhibited transformation to five-layered (10M) martensite structure between 297 to 328 K. All samples exhibited magnetic shape memory effect. Just below the transformation temperature the samples had very low twinning stress of about 0.1–0.3 MPa, which increased with decreasing temperature. The structural changes were monitored using X-ray diffraction in the temperature range 173–343 K. The 10M structure was approximated by monoclinic lattice with the unit cell derived from the cubic unit cell of the parent L2_1 phase. With decreasing temperature, the lattice parameters a and γ increased, c decreased, while b was nearly constant. For $x \leq 3.5$, sudden sharp changes in a and b parameters additionally occurred, resulting in $a = b$ in some regions of the phase diagram, which might be related to the refinement of twin structure of 10M martensite on nanoscale. The temperature dependences of lattice parameter γ (and c or c/a) correlate well with the temperature dependences of twinning stress in agreement with the prediction by a microstructural model of twin boundary motion. On the contrary, there is no correlation between $(a - b)$ and twinning stress. This indicates no significant role of a/b twins or laminate in twin boundary motion mechanism and low twinning stress.

Keywords: magnetic shape memory, X-ray diffraction, temperature dependence, twinning stress

*Corresponding author. Email: ladislav.straka@aalto.fi Phone: +358 50 415 2886

1 Introduction

Twinning stress is one of the most important parameter of magnetic shape memory alloys (MSMAs). Only with very low twinning stress the MSMAs can exhibit the giant straining in magnetic field mediated by the motion of martensite twin boundaries, which phenomenon is known as *magnetic shape memory effect* or *magnetically induced reorientation* (MIR) of martensite [1, 2, 3, 4, 5, 6, 7, 8, 9, 10]. The MIR can be utilized in applications requiring fast actuation with large strain [5], while the inverse MIR (modification of magnetic field by the ferromagnetic twin microstructure rearrangement) can be used for sensing-type applications or vibrational energy harvesting. It turns out that for good application performance the twinning stress must typically be as low as possible, of the order of 0.1 MPa [10, 11], or around 1 MPa in certain cases [12]. That is up to three orders lower than the twinning stress of ordinary shape memory materials [13].

The Ni-Mn-Ga based MSMAs with five-layered (10M) martensite structure demonstrate very low twinning stress, especially for the composition $\text{Ni}_{50}\text{Mn}_{25+x}\text{Ga}_{25-x}$, where $x = 2.7\text{--}3.9$ [10, 14]. The very low twinning stress of the order of 0.1 MPa or even 0.01 MPa [15] is observed with Type 2 martensite twin boundaries [16, 17, 18, 19, 20] in a broad temperature interval including room temperature [14, 21]. The Type 2 twin boundaries can form in 10M martensite because of the non-negligible monoclinicity of the nearly tetragonal lattice. They connect two martensite variants with different orientation of the c -axis by 180° lattice rotation around the twin shear axis. In contrast, the Type 1 twin boundaries [16, 17], connecting the two variants by a simple mirroring of the lattice at the twinning plane, show in average ≈ 1 MPa twinning stress at room temperature. The twinning stress further increases with decreasing temperature with the rate of about 0.04 MPa/K [21, 22].

The origin of the extraordinary low twinning stress in 10M martensite and sharply different twinning stress of Type 1 and Type 2 twin boundaries and twinning stress temperature dependences have not yet been fully explained, despite of the major significance of the subject for the whole field of MSMAs. Utilizing first-principles atomistic simulations and twin nucleation model based on the Peierls–Nabarro formulation, Wang and Sehitoglu [13] predicted twinning stress of 10M marten-

site to be 3.5 MPa, which is comparable to experimental value of ≈ 1 MPa for Type 1 twins. To explain the much lower twinning stress of Type 2 twins, Faran and Shilo [23] suggested that a thicker (more diffuse) Type 2 twin boundaries experience a smaller Peierls energy variation and thus require less driving force to move. Similar argument was presented by Kaufman et al. [24]. Heczko et al. [25], following reasoning by Salje and Lee et al. [26, 27], tentatively explained the very low twinning stress of Type 2 twins by flat potential energy landscape on an atomic scale.

Theoretical analysis of Rajasekhara and Ferreira [28], and more detailed analysis of Wang and Sehitoglu [13] and Faran and Shilo [29] show that the twinning stress depends on the shear modulus, the interplanar spacing between the twinning planes, and the Burgers vector of the twin dislocations. The latter two depend on the lattice parameters, and the lattice parameters, in turn, change significantly with temperature [30, 31, 32, 33]. In relation to lattice parameters it is also interesting to note that Sozinov et al. recently demonstrated that the twinning stress of tetragonal non-modulated (NM) martensite decreased significantly when reducing the c/a ratio, resulting in MIR in NM phase [7].

Seiner et al. [34] suggested that in addition to atomistic models (as e.g. Ref. [13]), also meso- and micro-structure should be considered as an important factor influencing the twinning stress. The particular internal twin microstructure can both decrease or increase the twinning stress considerably and can play important role in the different behavior of Type 1 and Type 2 twins. The developed microstructural model based on elastic continuum theory shows that especially the monoclinic distortion of the lattice represented by a difference in lattice parameters ($a - b$) and the monoclinic angle γ can control the twinning stress.

Thus, from various theoretical analyses and different experiments it seems that the increase of twinning stress with decreasing temperature can be related to the changes in lattice parameters. This motivated the present experimental investigation. It is important to note here that although the twin boundary kinetics in 10M martensite can depend strongly on thermal activation, the thermal activation may play no role in twinning stress [35]. For example very low $\approx 0.1\text{--}0.3$ MPa twinning stress of Type 2 twins down to 1.7 K was reported in Refs. [14, 22]. If there is no role of thermal activation, the direct

linking of twinning stress changes with changing lattice geometry or structure becomes highly relevant.

In this article, we investigate the links between the temperature-related increase in twinning stress and the lattice parameters using the direct measurements of both properties on the single crystals exhibiting MIR. We follow the changes of the structure with decreasing temperature in the same single crystals which exhibit the twinning stress of ≈ 0.1 MPa for Type 2 twins at room temperature. In order to take account of the effects of twin microstructure on twinning stress property, we pay a special attention to the changes in lattice monoclinicity, i.e. to the slight difference between a and b lattice axes and to the slight deviation of the related angle γ from 90° . The measured temperature dependences of the lattice parameters and changes in lattice monoclinicity are compared with the temperature dependences of twinning stress for Type 1 and Type 2 twin boundaries. Additionally we found previously unreported changes in structure manifested as sudden, non-monotonous changes in a and b lattice parameters.

2 Material and methods

Five $\text{Ni}_{50}\text{Mn}_{25+x}\text{Ga}_{25-x}$ alloys for the study, where x was between 2.7 and 3.9 at.%, Table 1, were produced by directional solidification in Adaptamat Ltd. The alloys were essentially the same as in our previous reports on the twinning stress [14, 22]. All alloys exhibited five-layered modulated (10M) martensite structure at room temperature. This structure is approximated in this study by a monoclinic lattice with the unit cell derived from the parent cubic $L2_1$ cell [36]. Using the monoclinic lattice allows to catch the main features of the structural changes without getting entangled into complexity and details of still disputed structure of 10M martensite. Limits of such approach are discussed later in subsection 3.5.

The cuboid single crystal samples of dimensions of $1 \times 2.5 \times 10 \text{ mm}^3$ and $1 \times 2.5 \times 20 \text{ mm}^3$ were cut from heat treated ingots along the $\{100\}$ planes. All crystals exhibited MIR at room temperature and very low twinning stress of ≈ 0.1 MPa for Type 2 and ≈ 1 MPa for Type 1 twins. The temperature dependences of twinning stress of alloys 1–5 were taken from Refs. [14] and [22], while the additional points for other alloys with $x = 2.7\text{--}3.9$ were taken from Ref. [21].

The nominal compositions of the alloys and the compositions determined using X-ray fluorescence (XRF) spectroscopy are given in Table 1 together with transformation temperatures. The main difference between the alloys is their Mn/Ga content, represented by x . Keeping the Ni content the same and as precisely as possible at 50 at.% is critical since the 10M phase region in Ni-content–temperature phase diagram becomes narrow at low temperatures [10]. Even a very small deviation of Ni content of the order of 0.1 at.% may result in enlarged twinning stress or instability of 10M martensite (see supplementary material of Ref. [14]). The magnetic and (inter)martensite transformation temperatures given in Table 1 were determined using AC and DC magnetic susceptibility measurements of the particular studied samples, and by complementary optical observations of twin bands (dis)appearance for the case of (reverse) martensite transformation.

The XRD measurements on single crystals were performed using two laboratory diffractometers with parallel beam optics and Euler cradle. We had to resort to non-usual X-ray analysis of single crystal in order to study precisely the same single crystals which exhibited the very low twinning stress and MIR. In previous study Mogyl'nyy et al. [18] demonstrated that on single crystals of 10M martensite the slight lattice monoclinicity can be seen well as the separation of the relevant diffraction lines such as (400) and (040), and (440) and ($\bar{4}40$) (adapted to our notation, originally (2 0 10) and (2 0 $\bar{1}0$), and (200) and (0 0 10)). The (400), (040) and (004) diffraction lines were measured in Bruker D8 Discover diffractometer equipped with rotating Cu anode ($\lambda = 0.1540598 \text{ nm}$) and cooling stage Anton Paar DCS 350. The stage temperature was varied from 350 K to 170 K. The (600), (060), (440), and ($\bar{4}40$) diffraction lines were measured in PANalytical X'Pert Pro diffractometer equipped with Co anode ($\lambda = 0.178901 \text{ nm}$) and in-house built heating/cooling stage based on Peltier element. The superstructure $\{600\}$ diffraction lines offer more precise lattice parameter determination than $\{400\}$ diffraction lines, but at the cost of small diffracted intensity (≈ 200 times lower than for $\{400\}$) [36]. In addition to limited amount of the lines, the precision of the structural parameters was limited by broadening of the martensitic peaks. The width of peaks was at least 0.2° compared to 0.09° for laboratory standard of Si single crystal.

Table 1: Nominal and XRFs-determined composition and transformation temperatures of the studied $\text{Ni}_{50}\text{Mn}_{25+x}\text{Ga}_{25-x}$ alloys: forward martensite transformation temperature $T_M \approx M_S \approx M_F$, reverse martensite transformation temperature $T_A \approx A_S \approx A_F$, forward IMT start temperature T_{IMT} , and reverse IMT start temperature T_{RIMT} . Equilibrium temperature was calculated as $T_0 = (T_{IMT} + T_{RIMT})/2$ for alloys 1–3, for Alloys 4 and 5 it was determined by extrapolation, see Ref. [14].

Alloy	x	Nominal composition	Composition by XRFs	T_M	T_A	T_{IMT}	T_{RIMT}	T_0
	(at. %)	(at. %)	(at. %)	(K)	(K)	(K)	(K)	(K)
Alloy 1	3.9	$\text{Ni}_{50.0}\text{Mn}_{28.9}\text{Ga}_{21.1}$	$\text{Ni}_{49.8}\text{Mn}_{29.4}\text{Ga}_{20.8}$	328	336	251	310	281
Alloy 2	3.7	$\text{Ni}_{50.0}\text{Mn}_{28.7}\text{Ga}_{21.3}$	$\text{Ni}_{50.2}\text{Mn}_{28.5}\text{Ga}_{21.3}$	324	330	182	287	235
Alloy 3	3.5	$\text{Ni}_{50.0}\text{Mn}_{28.5}\text{Ga}_{21.5}$	$\text{Ni}_{50.1}\text{Mn}_{28.4}\text{Ga}_{21.5}$	318	323	85	274	178
Alloy 4	3.2	$\text{Ni}_{50.0}\text{Mn}_{28.2}\text{Ga}_{21.8}$	$\text{Ni}_{50.0}\text{Mn}_{28.2}\text{Ga}_{21.8}$	309	315	10	<i>not resolved</i>	≈ 100
Alloy 5	2.7	$\text{Ni}_{50.0}\text{Mn}_{27.7}\text{Ga}_{22.3}$	$\text{Ni}_{50.0}\text{Mn}_{27.5}\text{Ga}_{22.5}$	297	301	<i>no IMT above 1.7 K</i>		≈ 0

To get unambiguous and as precise as possible lattice parameters we prepared samples with uniform orientation of c-axis ("single variant" state) by a few MPa compression, i.e., neither Type 1 nor Type 2 twin boundary was present during the XRD measurements. Nonetheless, the sample with this uniform orientation of c-axis still exhibits rich internal structure. It typically contains internal $\{100\}$ compound twins and internal $\{110\}$ compound twins, referred also as a/b -laminate and modulation domains, respectively [36, 37]. The unavoidable presence of the a/b -laminate allows to observe the (400) and (040) diffraction lines for single orientation of the sample; same applies also for the (600), (060) or (440), ($\bar{4}40$) pairs.

The diffraction maxima of the single crystals were first located using ω - and ψ - scans. Then the $\omega - 2\theta$ scans were measured with corresponding offsets. The obtained diffractograms were evaluated by in-house software that fitted up to six peaks using Pearson VII functions [38]. To achieve relevant precision, the peaks were fitted using K_α doublet. The width and shape parameters of Pearson VII function were constrained to have the same value for one diffractogram. That gave good stability of the fit when diffraction lines were overlapped at the cost of slightly reduced fit precision as the assumption of the same width for all diffraction lines was not fully justified.

In order to determine lattice parameter γ , we measured the $\{440\}$ diffraction lines as they are significantly influenced by this angle. In the monoclinic structure, the equation for the $\{hkl\}$ diffraction lines is [39]:

$$\frac{1}{d_{hkl}^2} = \frac{\frac{h^2}{a^2} + \frac{k^2}{b^2} - \frac{2hk \cos \gamma}{ab}}{\sin^2 \gamma} + \frac{l^2}{c^2}. \quad (1)$$

The two (440) and ($\bar{4}40$) diffraction lines in combination with (400) and (040) lines – or for increased precision (600) and (060) lines – provided all necessary information for γ determination. We had four independent measurements to determine three parameters: a , b , and γ . The interplanar distance d_{hkl} was calculated using Bragg's law $2d_{hkl} \sin \theta = n\lambda$. The search for $\{440\}$ diffraction lines, however, turned to be somewhat laborious when using powder diffractometers in single crystal studies. Therefore we developed a complementary method for γ determination, which utilized the fact that γ angle is closely related to the angle α observed between the traces of Type 1 and Type 2 twin boundaries on $\{100\}$ oriented surface [20] (see also Fig. 7):

$$\cos \gamma = \frac{c^2 - b^2}{2ab} \tan \alpha. \quad (2)$$

It is important to note here that even very small monoclinic distortion ($\gamma - 90^\circ$) of the order of 0.1° can result in relatively large angle α of the order of several degrees observed optically on the surface [20, 21, 36]. The temperature dependences of lattice parameters $a(T)$, $b(T)$, and $c(T)$ were determined from $\{400\}$ diffraction lines. The $\alpha(T)$ dependence was obtained from optical observations of sample with both Type 1 and Type 2 twin boundaries close to each other, using a light microscope equipped by an in-house built cooling/heating stage. Equation 2 is, however, valid only for ideal $\{101\}$ twins without internal structure. We assumed regular a/b -lamination, i.e. the same volume

fraction of a - and b -oriented lamellas ($\lambda = 0.5$ according to notation of Ref. [36]), and used a relevantly modified equation:

$$\gamma = \frac{1}{2} \arccos\left(\frac{c^2 - b^2}{2ab} \tan \alpha\right) + \frac{1}{2} \arccos\left(\frac{c^2 - a^2}{2ab} \tan \alpha\right) \quad (3)$$

Fine modulation domains can also lead to various tilt of Type 2 twin boundary and a false α reading [25, 40]. Nonetheless, in contrast to a/b -laminate, the modulation domains are often large enough (at least for crystals from Adaptamat) to be identified in optical microscope [36] and are also more easily controlled, for example by mechanical training [41]. We avoided the effect of modulation domains by preferably selecting samples with very large or nearly single modulation domain. In some cases, mechanical training consisting of tensile/compressive loadings was used to change the distribution of modulation domains towards the single domain configuration.

3 Results and discussion

In the following subsections 3.1 and 3.2 we describe in detail the study of two alloys (alloy 1 and 3) representing typical behavior and then we summarize all observations for all five alloys in subsections 3.3 and 3.4. In subsection 3.5 we discuss the limits of the used lattice approximation. The last two subsections 3.6 and 3.7 provide the comparison of structure evolution with the measured twinning stress. The first subsection 3.1 deals with simple case on which the validity of the structure determination method is demonstrated.

3.1 The 10M \leftrightarrow 14M \leftrightarrow NM transformation sequence observed in alloy 1

The magnetic susceptibility measured for alloy 1 during cooling and subsequent heating is shown in Fig. 1a. During cooling from 310 K, there are no significant changes in susceptibility down to $T_{IMT} = 251$ K, where a large sharp jump starts. This first jump in susceptibility is ascribed to the transformation to 14M martensite. During further cooling, start of second jump occurs at T_{IMT}^* , which marks the transformation of the 14M martensite to so-called non-modulated (NM, purely tetragonal) martensite with long c -axis. Upon following

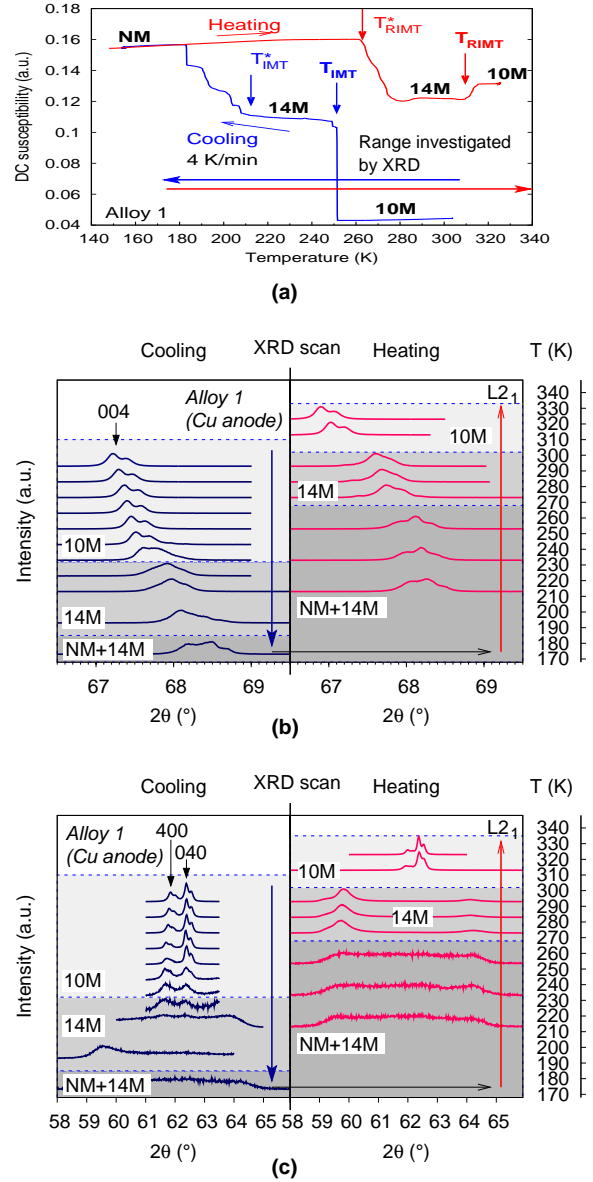


Figure 1: Structural changes in alloy 1: a) DC magnetic susceptibility curve with intermartensite transformation temperatures and corresponding phases 10M, 14M, NM marked. b, c) $\omega - 2\theta$ scans in selected 2θ intervals performed during quasistatic cooling and heating in temperature range marked in (a). The patterns are normalized to maximum intensity and positioned according to the measurement temperature (axis on the right). The {400} peaks of 10M phase and regions with different phases 10M, 14M, NM are marked. Peak splitting due to $K\alpha$ doublet is marked in Fig. 2b.

heating, the material exhibits again two sharp changes in susceptibility, ascribed to the reverse transformations NM \rightarrow 14M and 14M \rightarrow 10M at T_{RIMT}^* and T_{RIMT} , respectively. The different initial and final DC magnetic susceptibility for 10M martensite is easily explained by different twin variant distributions before and after the

transformations to other phases.

The $10M \leftrightarrow 14M \leftrightarrow NM$ intermartensite transformation (IMT) sequence is well known and was presented previously e.g. in [42, 43, 44]. As the temperature range investigated by XRD includes the IMTs of alloy 1, Fig. 1a, it is obvious that all the mentioned IMTs shall be reflected in the XRD patterns.

The thermal evolution of (004) peak in $\omega - 2\theta$ scans performed during cooling and heating is displayed in Fig. 1b. This and all below discussed diffraction peaks are split due to the presence of K_α doublet in the diffraction spectrum. During cooling from room temperature, the (004) peak shifts gradually, indicating the gradual shortening of the c lattice parameter. At 230 K, the peak broadens and then it shifts suddenly to the right at 220 K. That indicates $10M \rightarrow 14M$ transformation with the mixture of two phases being temporarily present around 230 K. The sudden shift to the larger 2θ marks the sudden contraction of the c lattice parameter and the finish of $10M \rightarrow 14M$ IMT (i.e., c_{10M} changed to c_{14M} and $c_{10M} > c_{14M}$).

Further cooling resulted in another change of the (004) peak shape at 170 K, at which temperature the peak consisted of two convoluted lines (not counting the K_α split). The new line at $2\theta \approx 68.5^\circ$ can be ascribed to NM phase; so there is a mixture of NM and 14M martensite at 170 K. Similarly as for the $10M \rightarrow 14M$ transformation, the NM phase exhibited slightly shorter lattice parameter than the 14M phase. Note that for NM martensite, the described "(004)" line actually corresponds to the $(400)_{NM}$ line and to the short a_{NM} lattice parameter (not to c_{NM} parameter). The different lattice parameters $c_{10M} > c_{14M} > a_{NM}$ indicate that the $10M \rightarrow 14M \rightarrow NM$ sequence can be induced also by an external compressive stress σ_{EXT} , since the stress will prefer the shorter lattice parameter of the other phase [44].

The observed transformation to NM martensite is, however, clearly incomplete. The magnetic susceptibility curve indicates that the whole $14M \rightarrow NM$ transformation occurs in about 30 K interval and sharply ends, Fig. 1a. Additional cooling beyond the limit of our experimental arrangement would presumably result in a pure NM phase. During heating from 170 K, the reverse transformations can be seen in the XRD pattern as the sudden shifts of (004) peak towards smaller 2θ , Fig. 1b. These shifts correspond to the reverse transfor-

mation sequence $NM(+14M) \rightarrow 14M \rightarrow 10M$, and to corresponding reverse changes of the relevant lattice parameter. The structural changes $10M \leftrightarrow 14M \leftrightarrow NM$ during cooling and heating are thus clearly demonstrated by the changes of the lattice parameter corresponding to the "(004)" peak, Fig. 1b.

The thermally-induced structural changes in alloy 1 are even more visible when monitoring the (400) and (040) diffraction lines, i.e. a and b lattice parameters of 10M martensite. The two reflections shift slightly with the decreasing temperature indicating gradual changes in a and b lattice parameters, but they suddenly disappear at about 230 K, Fig. 1c. Instead of these two reflections, two other lines appear at $2\theta \approx 59.5^\circ$ and at $2\theta \approx 64^\circ$. That corresponds very well to the $(400)_{14M}$ and $(040)_{14M}$ reflections, previously reported in the literature [8, 45, 46], and thus we can be quite confident that we really observe the 14M phase. Upon further cooling, these peaks almost disappear at 180 K due to the transformation to NM martensite. Upon following heating, the corresponding reverse transformations occur, resulting in reappearance of the relevant peaks, Fig. 1c.

In summary, we can conclude that alloy 1 exhibits behavior which is expected from the previously known $10M \leftrightarrow 14M \leftrightarrow NM$ transformation sequence. The changes in $\{400\}$ lines of 10M martensite or corresponding lines of the other phases reflect the thermally-induced changes in 10M lattice and also clearly indicate the IMTs of the $10M \leftrightarrow 14M \leftrightarrow NM$ sequence. The determined lattice parameters of the individual phases have relation $c_{10M} > c_{14M} > a_{NM}$. Importantly we observed also a mixture of $10M+14M$ and $14M+NM$ martensites, however, they were only present in limited temperature intervals. The confirmed behavior gave us the confidence that the used method is sound and can be applied to more complicated cases as shown below.

3.2 Temperature dependence of a , b , c lattice parameters in alloy 3

The magnetic susceptibility measured for alloy 3 during cooling and following heating is shown in Fig. 2a. The susceptibility curve exhibits similar features as the curve for alloy 1 indicating the $10M \leftrightarrow 14M \leftrightarrow NM$ transformation sequence, but the transformations are shifted to much lower temperature and are less clearly sepa-

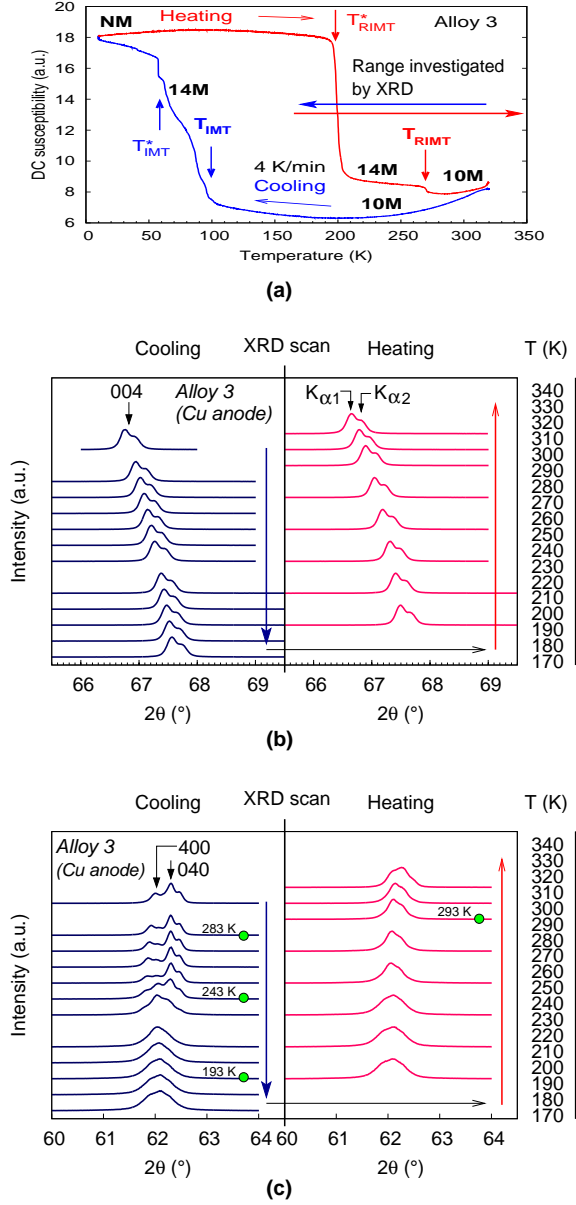


Figure 2: Structural changes in alloy 3: a) DC magnetic susceptibility with ascribed intermartensite transformation temperatures and corresponding phases 10M, 14M, NM marked. b, c) $\omega - 2\theta$ scans in selected 2θ intervals performed during quasistatic cooling and heating in temperature range marked in (a). The patterns are normalized to maximum intensity and are positioned according to the measurement temperature (axis on the right). The $\{400\}$ peaks of 10M phase and peak splitting due to K_{α} doublet are marked.

rated. The intermartensite transformation temperatures T_{IMT} and T_{IMT}^* are well below the interval available in the X-ray diffraction measurement and thus none of the $10M \leftrightarrow 14M \leftrightarrow NM$ IMTs can be seen in the XRD patterns.

The (004) peak for alloy 3 monitored during cool-

ing and heating is shown in Fig. 2b. The peak gradually shifts with temperature indicating the gradual changes in c lattice parameter, but there are no sudden shifts as those observed for alloy 1. That is an additional indication that none of the $10M \leftrightarrow 14M \leftrightarrow NM$ transformations occurs. Nonetheless, some subtle changes in structure appear, reflected as changes in (400) and (040) peaks, described below. During cooling, the (400) and (040) peaks only shift slightly with the decreasing temperature at first, Fig. 2c. At 243 K, the peaks suddenly start changing their shape, and at even lower temperature, the two peaks (400) and (040) merge into a single broad peak which looks almost featureless. During the following heating, this broad peak changes only slightly its shape but does not visibly split.

Closer analysis of the selected XRD patterns obtained at 283, 243, and 193 K upon cooling and at 293 K upon heating (marked in Fig. 2c by filled green circles) is shown in Fig. 3. The analysis reveals that in addition to the two (400) and (040) lines observed e.g. at 283 K, Fig. 3a, a third line appears around 243 K, Fig. 3b. With the temperature decreasing further, this new peak gains intensity on the account of the original (400) peak, Fig. 3c. We assign a' lattice parameter to this new line, where $a > a' > b$. As we monitor only few peaks, we cannot decide here whether the new line reflects the growth of “new” martensitic phase or if the same lattice is showing a new type of distortion. The detailed analysis using synchrotron radiation is planned to clarify the issue. Upon following heating from low temperatures, the peak shape also changes with temperature, and the analysis indicates that at 273 K, the XRD pattern can be fit by only a single peak, corresponding to a common lattice constant $a = b$.

Thus, we observe some kind of structural transformation which results in sudden small sharp changes of a and b lattice parameters but importantly not of c parameter. Similar XRD pattern developments, corresponding to sudden sharp changes in a and b or to $a = b$, were observed also in alloys 4 and 5. In these cases, however, no third peak was found. All observations are summarized and discussed in the next chapter.

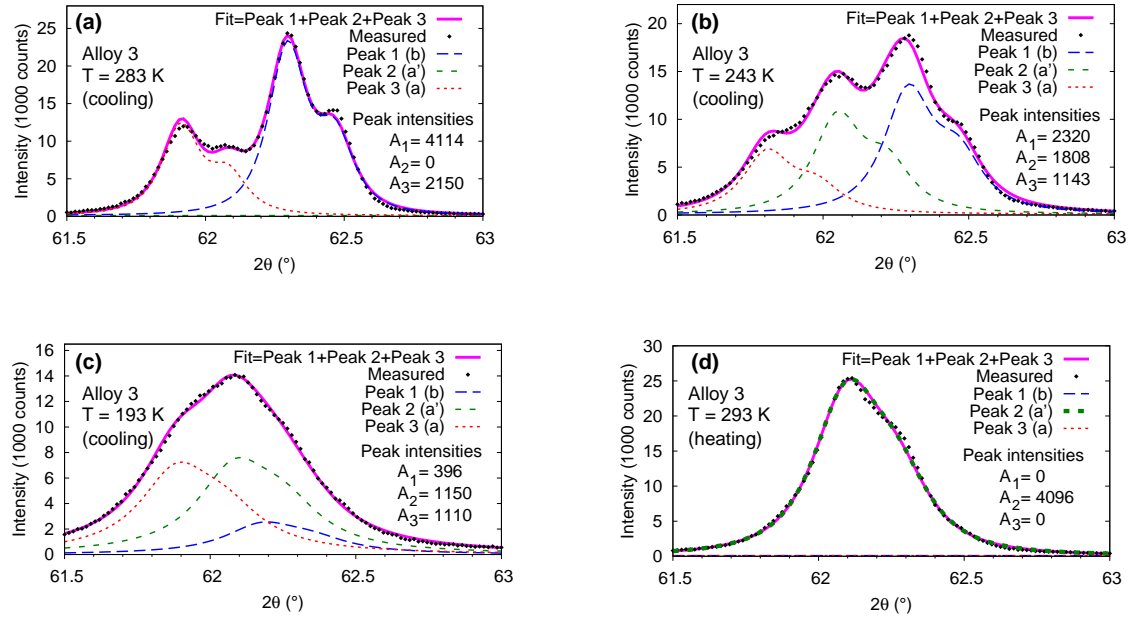


Figure 3: The closer look and fitting of selected XRD patterns (marked by green filled circles in Fig. 2) using Pearson VII function: a) alloy 3 at 283 K, cooling; b) alloy 3 at 243 K, cooling; c) alloy 3 at 193 K, cooling; d) alloy 3 at 293 K, heating. The provided peak intensities are normalized to Lorentz polarization factor (≈ 5).

3.3 Temperature dependence of a, b, c lattice parameters summarized for all alloys

The room temperature a, b lattice constants determined during cooling are summarized in Fig. 4a. In agreement with the previous investigation by Lanska et al. [30], the difference between a and b decreases when the (reverse) martensite transformation temperature approaches the room temperature.

The a and b lattice parameters of all alloys as functions of temperature are displayed in Fig. 4b-f. Alloy 1 exhibits small gradual changes of the parameters with temperature, Fig. 4b, with b almost constant and a rising slightly with decreasing temperature. Pagounis et al. reported recently same trends in the lattice constants for $\text{Ni}_{50}\text{Mn}_{29.2}\text{Ga}_{20.8}$, which is very close to alloy 1 [31]. Alloy 2 exhibits similar dependence, but the parameters show some tendency to come closer to each other at about 220 K upon cooling and at about 270 K upon heating, Fig. 4c. In alloy 4, the parameters seem to actually coincide at about 270 K upon cooling and separate at about 300 K upon heating, but there is also a weak line corresponding to the original (400) line or a parameter, with decreasing intensity, Fig. 4e. Similar coincidence of parameters upon cooling is ob-

served in alloy 5, in which, however, no weak line is observed and the parameters are so close to each other that they can be distinguished only by using $\{600\}$ diffraction lines, which provide better resolution than $\{400\}$, Fig. 4f. Unfortunately the analysis using $\{600\}$ lines was only possible near room temperature in our experimental arrangement.

Alloy 3 exhibits complex development of lattice constants, Fig. 4d, which may be a combination of the effects observed in alloys 2 and 4. Upon cooling, the parameters come closer to each other at about 260 K (but do not coincide) while there is still an extra weak line corresponding to the original (400) reflection. During heating, the parameters eventually coincide at 250 K and then separate around 320 K (see also peak analysis in Fig. 3). In repeated experiments, the weak lines were sometimes undetected in alloys 3 and 4, which may be due to different analyzed spot or sample adjustment.

In contrast to complex changes observed for a, b lattice parameters, the c lattice parameter exhibits rather uniform behavior in all alloys. The dependence of c lattice parameter of 10M martensite on the relative temperature ($T - A_S$) is similar in all alloys studied, Fig. 5; the parameter decreases gradually with decreasing temperature.

Based on a, b, c lattice parameters evolution obtained

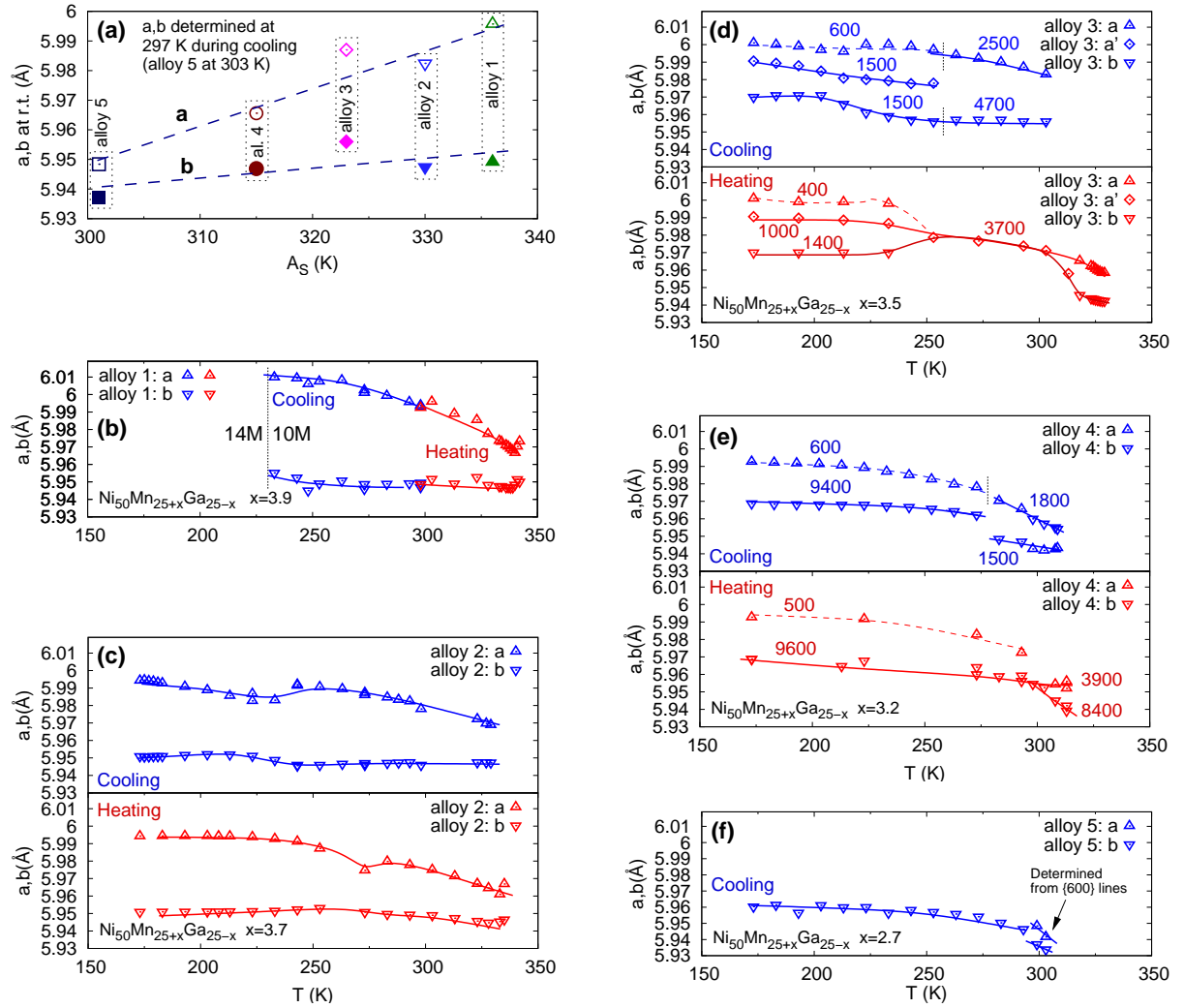


Figure 4: Temperature dependences of a, b lattice parameters summarized for alloys 1–5: a) Room temperature a, b lattice parameters as functions of austenite start (A_S) temperature. b-f) Determined temperature dependences of a, b lattice parameters for alloy 1 (b), alloy 2 (c), alloy 3 (d), alloy 4 (e), and alloy 5 (f). The numbers next to selected curves are average peak intensities (counts) of the relevant curve parts. Dashed and solid lines are just guides for eyes.

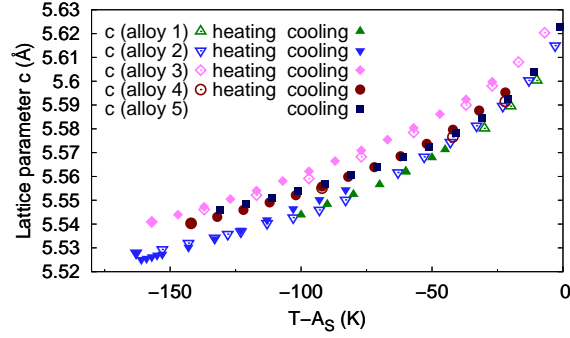


Figure 5: Lattice parameter c as a function of relative temperature ($T - A_s$) for alloys 1–5.

from the peak analysis, we can state rather confidently that some significant changes in 10M structure related only to a and b lattice parameters occur in alloys 3 and 4 upon heating and cooling. The approximate temperature and compositional region of this “new phase” and of phase with $a = b$ is marked by the green area in the phase diagram in Fig. 6. New phases were reported in Ni-Mn-Ga before; for example Kim et al. [47] and Kushida et al. [48] indicated new “x-phase” induced in austenite or pre-martensite by compressive stress. However, as we investigate only few lines of a single crystal diffraction pattern, we cannot provide full explanation of the new structure formed. That is beyond the scope of this article and requires further research. Here we can only suggest that for certain composition and temperature ranges, the material transforms to a slightly modified or “new” 10M phase. In our monoclinic approximation this phase exhibits a close to or it is even identical to b (corresponding to the strong a' or b lines at low temperatures in Fig. 4d-f), while the residua of the original phase with $a \neq b$ remain in the material (and generate the weak (400) or a line). See section 3.5 for further discussion.

3.4 Temperature dependence of γ lattice parameter

The γ lattice parameter was determined by two methods: from {440} reflections (Eq. 1) and from optical observations of the angle α between the Type 1 and Type 2 twin boundary traces on the {100} surface (insets in Fig. 7a and Eq. 3). The evident change of angle α with temperature is demonstrated for alloy 1 in Fig. 7a. The α angle decreases with increasing temper-

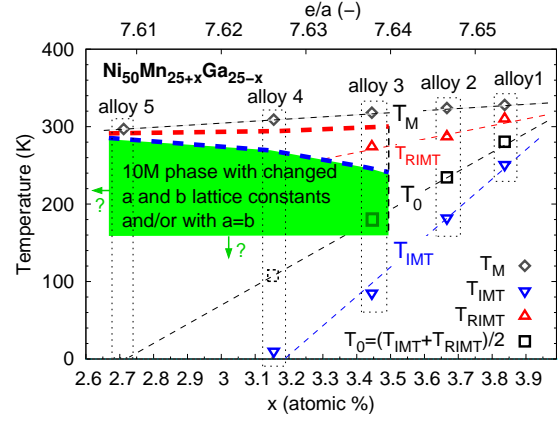
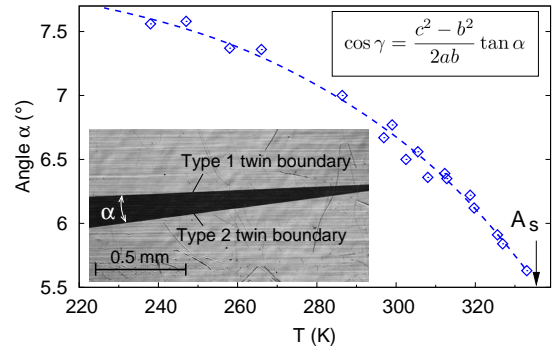
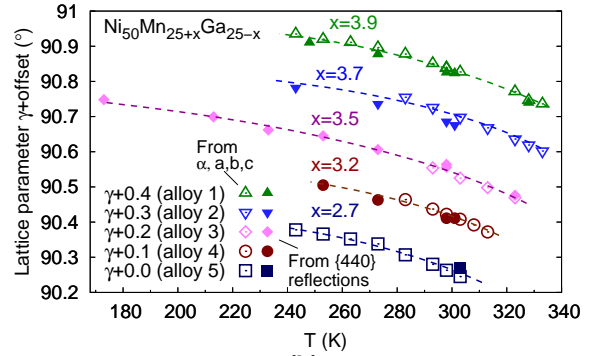


Figure 6: Phase diagram showing the region with “new phase” with changed a, b lattice parameters and/or with $a = b$. The region is marked by green color and thick dashed blue line (changes in a, b occurring on cooling) and red line (changes in a, b occurring on heating).



(a)



(b)

Figure 7: Measurements related to γ lattice parameter: a) Angle α as a function of temperature in alloy 1, determined as illustrated in the lower inset. The principal relation between α and γ is given in the upper inset. b) Lattice parameter γ (+offset) as a function of temperature determined from {440} reflections, Eq. 1 (filled symbols) and from α , Eq. 3 (empty symbols) for alloys 1–5. Note various 0–0.4° offset added to the dependences for the sake of clarity, for an alternative offset-free plot, see Fig. 8c.

ature in all alloys. However, even very near (reverse) martensite transformation it is far from zero in all alloys, indicating that γ deviates from 90° even just prior to reverse transformation.

To demonstrate equivalence between two approaches the comparison is made in Fig. 7b; the filled symbols were determined using Eq. 1, while the open symbols by Eq. 3. It is apparent that both methods yield very similar values of γ . In order to facilitate the comparison with the twinning stress, an alternative plot of γ as a function of relative temperature $T - A_S$ is shown in Fig. 8c. All alloys exhibit very similar $\gamma(T - A_S)$ dependence with γ decreasing with increasing temperature. Near martensite transformation, $\gamma \approx 90.25^\circ$, while 50 K below the transformation, $\gamma \approx 90.4^\circ$.

3.5 Limits of the used lattice approximation

The used monoclinic lattice approximation and description by a, b, c, γ lattice constants cannot in principle describe fully the 10M structure and its fine structural changes. The changes in diffraction patterns observed in monoclinic approximation as sudden changes in a, b lattice constants may originate also from other effects than the simple change in lattice symmetry. These may be, for example, refinement in the a/b -lamination, changes in twinning periodicity, changes in stacking of basal planes of 10M structure, or, more generally, as refining or coarsening of adaptive martensite [24, 46]. Recently Ge et al. [49] demonstrated gradual change of lattice parameters resulting from the coarsening of nanotwins during the 14M \rightarrow NM transformation observed by TEM. All the mentioned effects can significantly influence the diffraction pattern and can result in an additional or missing diffraction peaks and consequent difficulties in lattice symmetry determination [50, 51].

In this respect it is also interesting to note that according to Righi et al. [52], the transformation of the 10M structure from commensurate to incommensurate did not result in sudden changes in a, b lattice constants. Additionally Glavatsky [33] reported magnetic transitions in the 10M structure, but did not find any sudden changes in lattice constants. In our case, the observed structural transitions do not seem to be of magnetic character, since we did not detect any significant changes in magnetic susceptibility during the sudden

small changes in a, b lattice parameters (compare Fig. 2a and Fig. 2c at 240 K).

3.6 Relation between lattice parameters and twinning stress for Type 1 twins

For all alloys in the studied composition range, the twinning stress of Type 1 twins increases rapidly with decreasing temperature following an universal dependence with the slope of about 0.04 MPa/K [22, 21]. This dependence is displayed in Fig. 8a by open blue diamonds (alloy 5) and small filled red squares (various alloys from [21] with $x = 2.7 - 3.9$), and is labeled as "Type 1 twins". The microstructural model by Seiner et al. [34] suggests that the increase originates from the a/b -lamination ($\{110\}$ compound twins) and thus it is related to the difference between the a and b lattice constants ($a - b$). Alternatively, it can originate from modulation domains ($\{100\}$ compound twins) and thus it is related to angle γ , or, more precisely, to $\gamma - 90^\circ$.

The determined $(a - b)$ as a function of relative temperature ($T - A_S$) is given in Fig. 8b. In spite of some scatter, it is obvious from the figure that the $(a - b)$ dependences differ significantly for different alloys. The higher is the transformation temperature (or Mn content of the alloy or electron per atom concentration e/a), the larger is the $(a - b)$ difference and it grows more rapidly with the decreasing temperature. For alloys with transformation close to room temperature (alloys 4 and 5), the $(a - b)$ difference is nearly zero or zero in most of the temperature intervals studied, see also Fig. 4e, f.

The significantly different $(a - b)$ dependences in different alloys, Fig. 8b, compared with the same universal dependence of twinning stress for Type 1 twins, Fig. 8a, indicate that the increase in twinning stress cannot originate from the a/b lamination. Especially for alloy 5, the a and b are very close to each other or identical resulting in no a/b -laminate, but the twinning stress increase is about the same as in other alloys (note that incorrect a, b constants were listed in Ref. [22] due to an unnoticed typo). Thus, this experiment excludes the a/b -lamination as the primary origin of the twinning stress increase for Type 1 twins.

In contrast, better correlation is obtained with the $\gamma(T - A_S)$ dependences. All alloys exhibit similar $\gamma(T - A_S)$ dependences in the temperature interval between A_S and at least $A_S - 50$ K, Fig. 8c. That compares well,

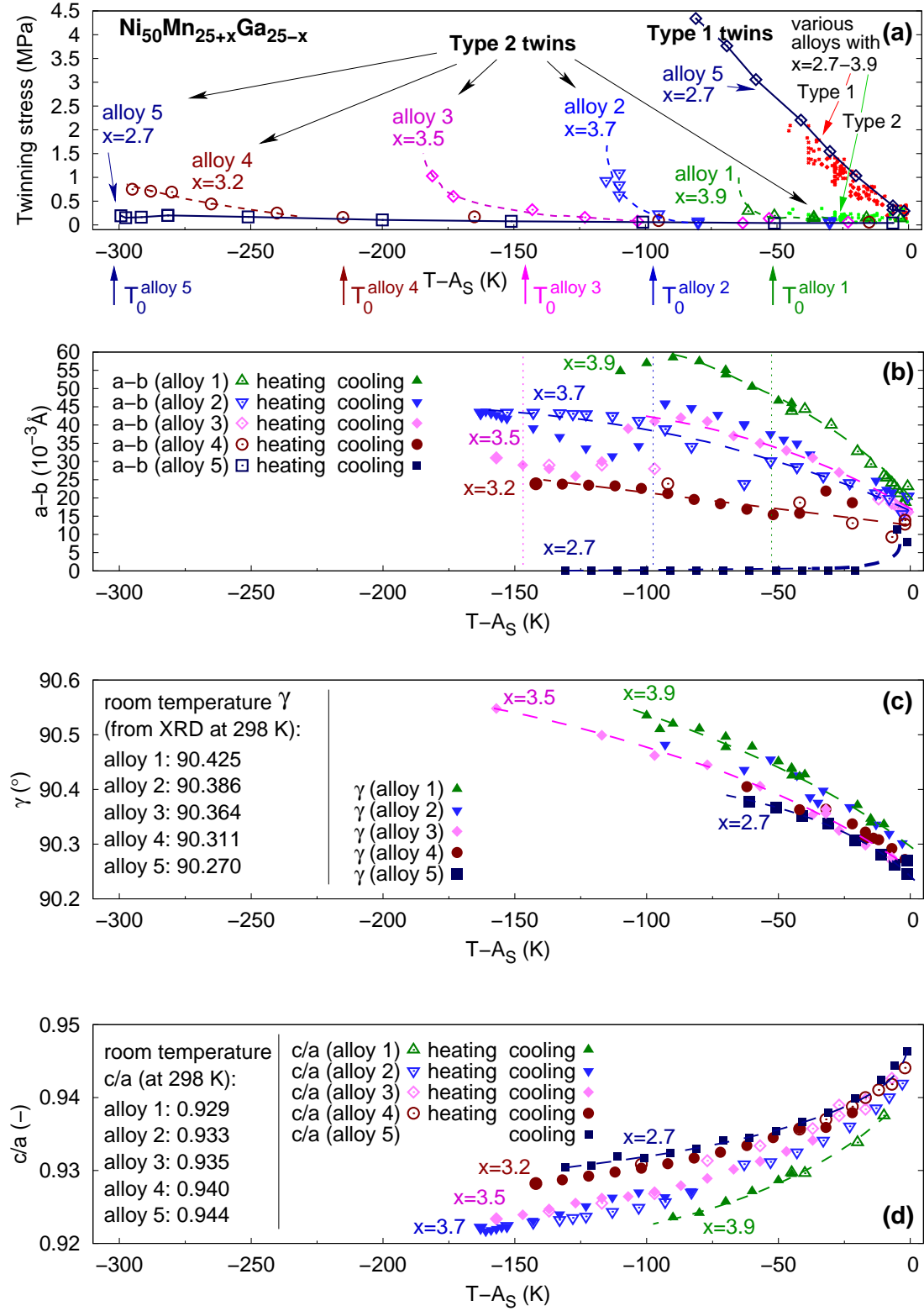


Figure 8: Comparison of twinning stress temperature dependences (a) with the temperature dependences of lattice parameters ($a-b$) (b), γ (c), and c/a (d). The temperature is given relative to the austenite start temperature (A_S); $T_0 = (T_{IMT} + T_{RIMT})/2$ marks the equilibrium temperature. The twinning stress dependences are compiled from our previous measurements presented in Refs. [14] (alloy 1–5, Type 2 twins), [22] (alloy 5, Type 1 twins), and [21] (Type 1 and Type 2 twins, red and green filled squares). Room temperature γ and c/a are additionally listed in insets in (c) and (d). Dashed and solid lines are guides for eyes only.

within the experimental scatter, with the observed universal dependence of twinning stress of Type 1 twins, Fig. 8a. This suggests that the increase in twinning stress may originate from the $\gamma - 90^\circ$ distortion. According to the theoretical model [34] and experimental investigations [37], the propagating Type 1 twin boundary interacts strongly with modulation domains ($\{100\}$ compound twins). The modulation domains may be distributed in bulk or may be formed in the vicinity of the propagating boundary [37]. Larger $\gamma - 90^\circ$ means that more energy is needed to form, overcome or redistribute the modulation twins, so the positive correlation between γ and twinning stress is expected [34].

Moreover, the c lattice parameter or c/a ratio exhibits similar dependence in all alloys, Figs. 5 and 8d. This can be significant because the c/a ratio represents the twinning shear, which must somehow influence the twinning stress. For example in doped NM martensite the twinning stress decreased about tenfold when c/a was reduced by about 5% [7]. Thus, the observed increase of twinning stress with decreasing temperature may be potentially linked to the changes in c or c/a . Nonetheless, c/a as a function of $(T - A_S)$ is slightly different in different alloys, Fig. 8d, and its correlation with twinning stress is slightly less convincing than for the case of γ .

3.7 Relation between lattice parameters and twinning stress for Type 2 twins

The temperature dependences of twinning stress for Type 2 twins are given in Fig. 8a for each alloy separately and additionally the observations for various alloys from [21] with $x = 2.7 - 3.9$ are given as small filled green squares. The dependences are labeled as "Type 2 twins" in the figure. The twinning stress is about constant between A_S and some (low) temperature, below which it rises rapidly. This temperature depends on alloy composition and was found to coincide with the equilibrium temperature $T_0 = (T_{IMT} + T_{RIMT})/2$, which suggests that the twinning stress rise is related to the emerging embryos of the 14M phase [14]. Alternatively it was suggested that the rise may also originate from changes in the lattice constants and thus we compare here the lattice constants and twinning stress. The comparison can be made only for alloys 1 and 2 and partly for alloy 3; the rest of alloys exhibit the increase in twinning

stress below the measured temperature range.

No systematic correlation can be seen between the Type 2 twinning stress increase and changes in lattice constants, Fig. 8. No significant changes in lattice parameters of alloy 1 occur at T_0 where the twinning stress starts rising. In contrast, alloy 2 exhibits sudden changes in a, b lattice parameters near T_0 . Nonetheless, alloy 3 shows similar sudden changes in lattice parameters far above the T_0 , with no impact on the twinning stress. Thus, there is no clear correlation with the lattice constants, and the emerging embryos of the 14M phase remain to be the most suspected reason for increasing twinning stress of Type 2 twins.

4 Conclusions

The temperature dependences of lattice parameters a, b, c , and γ were determined for $\text{Ni}_{50}\text{Mn}_{25+x}\text{Ga}_{25-x}$ single crystals with 10M structure exhibiting very low twinning stress and magnetically induced reorientation (MIR). With decreasing temperature, the lattice parameters a and monoclinic angle γ increased, c decreased, while b was nearly constant. Sudden large changes of lattice parameters indicate the intermartensite transformation sequence $10\text{M} \leftrightarrow 14\text{M} \leftrightarrow \text{NM}$. Additionally, in alloys with $x \leq 3.5$, we observed small sudden changes in a, b lattice parameters (but not in c parameter) far above the intermartensite transformation temperature. This suggests some fine structural rearrangement of 10M martensite, which may be related to the refinement of twin structure on nanoscale.

The direct comparison of the determined temperature dependences of lattice parameters with the temperature dependence of twinning stress indicate the following:

- Twinning stress of Type 1 twin boundaries is not correlated with $(a - b)$, but it is reasonably correlated with γ , and there is also a reasonable correlation with c or c/a .
- Twinning stress of Type 2 twin boundaries is not correlated with any of the studied lattice parameters.

Thus, in contrast with the microstructural model [34], the twinning stress of Type 1 twin boundaries does not depend significantly on a/b lamination. On the other

hand, an alternative suggestion of the model that γ controls the twinning stress of Type 1 twin boundaries is in agreement with our experiment. The observed correlation with c/a may be also relevant [7] and should be considered in the future models of twinning stress and MIR.

Acknowledgment

This work was funded by the Academy of Finland, Czech Scientific Foundation project of excellence No. 14-36566G, and by Academy of Sciences of the Czech Republic in grant for international cooperation No. M100101241. K.R. thanks for support of CSF grant No. P107/11/0391. The authors thank Adaptamat Ltd. for providing samples for investigation and to Alexei Sozinov for fruitful discussions.

References

- [1] Webster PJ, Ziebeck KRA, Town SL, Peak MS. *Phil. Mag. B* 49 (1984) 295.
- [2] Ullakko K, Huang JK, Kantner C, O'Handley RC, Kokorin VV. *Appl Phys Lett* 69 (1996) 1966.
- [3] Söderberg O, Sozinov A, Ge Y, Hannula S-P, Lindroos VK. Giant magnetostrictive materials, in Buschow J (ed.). *Handbook of Magnetic Materials*, Elsevier Science, Amsterdam 16 (2006) 1.
- [4] Heczko O, Scheerbaum N, Gutfleisch O. Magnetic shape memory phenomena in: Liu JP, Fullerton E, Gutfleisch O, Sellmyer DJ (Eds.). *Nanoscale Magnetic Materials and Applications*, Springer US (2009) 399.
- [5] Wilson SA, Jourdain RPJ, Zhang Q, Dorey RA, et al. *Mat Sci Eng R: Reports* 56 (2007) 1.
- [6] Likhachev AA, Sozinov A, Ullakko K. *Mech Mat* 38 (2006) 551.
- [7] Sozinov A, Lanska N, Soroka A, Zou W. *App Phys Lett* 102 (2013) 021902.
- [8] Sozinov A, Likhachev AA, Lanska N, Ullakko K. *App Phys Lett* 80 (2002) 1746.
- [9] Karaca HE, Karaman I, Basaran B, Chumlyakov YI, Maier HJ. *Acta Mat* 54 (2006) 233.
- [10] Straka L, Hänninen H, Soroka A, Sozinov A. *J Phys: Conf Ser* 303 (2011) 012079.
- [11] Schmidt H, *J Phys: Conf Ser* 303 (2011) 012078.
- [12] Schlüter K, Holz B, Raatz A, *Adv Eng Mat* 14 (2012) 682.
- [13] Wang J, Sehitoglu H. *Acta Mat* 61 (2013) 6790.
- [14] Straka L, Sozinov A, Drahokoupil J, Kopecký V, Hänninen H, Heczko O. *J App Phys* 114 (2013) 063504.
- [15] Kellis D, Smith A, Ullakko K, Müllner P. *J Crystal Growth* 359 (2012) 64.
- [16] M. A. Jaswon and D. B. Dove, *Acta Crystallogr.* 13 (1960) 232.
- [17] B. A. Bilby, A. G. Crocker, *Proc. R. Soc. Lond. A* 288 (1965) 240.
- [18] Mogilyny G, Glavatsky I, Glavatska N, Soderberg O, Ge Y, Lindroos VK. *Scripta Mat* 48 (2003) 1427.
- [19] Nishida M, Hara T, Matsuda M, Ii S, *Mat Sci Eng A* 481–482 (2008) 18.
- [20] Sozinov A, Lanska N, Soroka A, Straka L, *App Phys Lett* 99 (2011) 124103.
- [21] Straka L, Soroka A, Seiner H, Hänninen H, Sozinov A. *Scripta Mat* 67 (2012) 25.
- [22] Heczko O, Kopecký V, Sozinov A, Straka L, *App Phys Lett* 103 (2013) 072405.
- [23] Faran E, Shilo D. *J Mech Phys Sol* 59 (2011) 975.
- [24] Kaufmann S, Niemann R, Thersleff T, Rößler UK, Heczko O, Buschbeck J, Holzapfel B, Schultz L, Fähler S. *New J Phys* 13 (2011) 053029.
- [25] Heczko O, Straka L, Seiner H. *Acta Mat* 61 (2013) 622.
- [26] Salje EKH. *Phase Transitions* 83 (2010) 657.
- [27] Lee WT, Salje EKH, Goncalves-Ferreira L, Daraktchiev M, Bismayer U. *Phys Rev B* 73 (2006) 214110.
- [28] Rajasekhara S, Ferreira PJ. *Scripta Mat* 53 (2005) 817.

- [29] Faran E, Shilo D. *J Mech Phys Sol* 61 (2013) 726.
- [30] Lanska N, Soderberg O, Sozinov A, Ge Y, Ulakko K, Lindroos VK. *J App Phys* 95 (2004) 8074.
- [31] Pagounis E, Chulist, Szczerba MJ, Laufenberg M, *Appl. Phys. Lett.* 105 (2014) 052405.
- [32] Glavatska N, Mogilniy G, Glavatsky I, Danilkin S, Hohlwein D, Beskrovnij A, Söderberg O, Lindroos VK. *J. Phys IV France* 113 (2003) 963.
- [33] Glavatsky I, Glavatska N, Urubkov I, Hoffman J-U, Bourdarot F, *Mat Sci Eng A* 481–482 (2008) 298.
- [34] Seiner H, Straka L, Heczko O, *J Mech Phys Sol* 64 (2014) 198.
- [35] Faran E, Shilo D, *Mat Sci Tech* 30 (2014) 1545.
- [36] Straka L, Heczko O, Seiner H, Lanska N, Drahoukoupil J, Soroka A, Fähler S, Hänninen H, Sozinov A, *Acta Mat* 59 (2011) 7450.
- [37] Chulist R, Straka L, Lanska N, Soroka A, Sozinov A, Skrotzki W, *Acta Mat* 61 (2013) 1913.
- [38] Prevéry PS. *Adv X-Ray Anal* 29 (1986) 103.
- [39] Cullity BD, Stock SR. *Elements of X-ray Diffraction*, third ed., Upper Saddle River, NJ:Prentice Hall (2001).
- [40] Heczko O, Kopeček J, Straka L, Seiner H, *Mat Res Bull* 48 (2013) 5105.
- [41] Chulist R, Straka L, Sozinov A, Lippmann T, Skrotzki W. *Scripta Mat* 68 (2013) 671.
- [42] Seguí C, Chernenko VA, Pons J, Cesari E, Khovailo V, Takagi T. *Acta Mat* 53 (2005) 111.
- [43] Seguí C, Pons J, Cesari E, *Acta Mat* 55 (2007) 1649.
- [44] Chernenko VA, Pons J, Cesari E, Ishikawa K, *Acta Mat* 53 (2005) 5071.
- [45] Çakır A, Righi L, Albertini F, Acet M, Farle M, Aktürk S, *J Appl Phys* 114 (2013) 183912.
- [46] Kaufmann S, Röbner UK, Heczko O, Wuttig M, Buschbeck J, Schultz L, Fähler S, *Phys Rev Lett* 104 (2010) 145702.
- [47] Kim J-H, Fukuda T, Kakeshita T, *Scripta Mat* 54 (2006) 585.
- [48] Kushida H, Hata K, Fukuda T, Terai T, Kakeshita T, *Scripta Mat* 60 (2009) 96.
- [49] Ge Y, Zarubova N, Heczko O, Hannula S-P, "TEM in-situ observation of stress induced transition from modulated to non-modulated martensite in Ni-Mn-Ga alloy", submitted to *Acta Materialia*, 2014.
- [50] Ustinov A, Olikhovska L, Glavatska N, Glavatsky I, *J Phys: Conf Ser* 226 (2010) 012016.
- [51] Olikhovska L, Ustinov A, Glavatska N, Glavatsky I, *Esomat 2009* (2009) 02025. DOI:10.1051/esomat/200902025.
- [52] Righi L, Albertini F, Paoluzi A, Fabbri S, Villa E, Calestani G, Besseghini S. *Mat Sci Forum* 635 (2010) 33.